Immiscible three-dimensional fingering in porous media: A weakly nonlinear analysis

Rodolfo Brandão, Eduardo O. Dias, and José A. Miranda*
Departamento de Física, Universidade Federal de Pernambuco, Recife, Pernambuco 50670-901, Brazil

(Received 19 October 2017; published 28 March 2018)

We present a weakly nonlinear theory for the development of fingering instabilities that arise at the interface between two immiscible viscous fluids flowing radially outward in a uniform three-dimensional (3D) porous medium. By employing a perturbative second-order mode-coupling scheme, we investigate the linear stability of the system as well as the emergence of intrinsically nonlinear finger branching events in this 3D environment. At the linear stage, we find several differences between the 3D radial fingering and its 2D counterpart (usual Saffman-Taylor flow in radial Hele-Shaw cells). These include the algebraic growth of disturbances and the existence of regions of absolute stability for finite values of viscosity contrast and capillary number in the 3D system. On the nonlinear level, our main focus is to get analytical insight into the physical mechanism resulting in the occurrence of finger tip-splitting phenomena. In this context, we show that the underlying mechanism leading to 3D tip splitting relies on the coupling between the fundamental interface modes and their first harmonics. However, we find that in three dimensions, in contrast to the usual 2D fingering structures normally encountered in radial Hele-Shaw flows, tip splitting into three branches can also be observed.

DOI: 10.1103/PhysRevFluids.3.034002

I. INTRODUCTION

Viscous fingering [1] occurs whenever a less viscous fluid displaces a more viscous one in either a three-dimensional (3D) or 2D porous medium or yet in a quasi-2D geometry of a Hele-Shaw cell. In all these situations, the less viscous fluid pushes through the more viscous fluid, creating small disturbances on the fluid-fluid interface that grow in time and propagate, assuming fingerlike shapes (the so-called viscous fingers). These fingering structures penetrate further into the more viscous fluid, leading to the formation of complex interfacial patterns.

The phenomenon of viscous fingering was first studied by Hill [2] in applied research connected to the sugar refining industry. However, the seminal work of Saffman and Taylor [3] laid the foundation of the field, through their experimental and theoretical investigations of 2D viscous fingering in Hele-Shaw cells. The basic practical motivation for the work carried out by Saffman and Taylor was actually to study physical events that take place during oil extraction in real life 3D porous media. In this context, they have shown that the effectively 2D Hele-Shaw cell device was a useful tool to be used as a laboratory model for flow in 3D porous rocks because both flows are governed by the same equation of motion, namely, Darcy's law [4]. It is worthwhile to note that the analytical work in Saffman and Taylor's original paper was also performed and published independently by Chuoke *et al.* [5] and by Zhuravlev [6].

Since the establishment of this influential set of works [2,3,5,6], the study of viscous fingering thus has a bearing on a number of scientific and technological problems. On the practical side, it is related

*jme@df.ufpe.br

to many industrial and geological processes, such as oil recovery [7] and CO_2 geological sequestration [8]. On the academic side, viscous fingering became an archetype for a wide spectrum of pattern formation systems, including dendritic solidification [9], flame propagation [10], and microdischarges in plasmas [11], biodynamics of cell fragmentation [12,13], and growth of bacterial colonies [14].

A large number of investigations on viscous fingering focus on experiments, analytical calculations, and numerical simulations in the confined environment of a Hele-Shaw cell [1]. This cell is a quasi-2D apparatus where fluids are confined between two parallel glass plates whose narrow gap spacing is smaller than any other length scale in the problem. Most of the 2D viscous fingering studies concentrate on two basic Hele-Shaw cell geometries: rectangular [3,15–22] and radial [23–39]. In the rectangular (or channel) geometry, fluids flow uniformly across the width of the channel, ultimately leading to the formation of a single, long, smooth steady-state finger. In contrast, in the radial (or circular) geometry setup an inner less viscous fluid is injected at the center of the cell, displacing an outer more viscous fluid radially outward. This radial spreading of the two-fluid interface induces the development of several fingers that subsequently extend and expand, eventually splitting at their tips. This tip-splitting instability can repeat itself multiple times to create very ornate and complicated fractal-like interfacial patterns. In fact, one can say that the tip-splitting phenomenon is the most emblematic pattern-formation process in 2D viscous fingering.

In contrast to the 2D fingering studies in Hele-Shaw cells that consider displacements under both immiscible and miscible circumstances, a greater number of the investigations of 3D fingering in porous media address flow of miscible fluids. As a matter of fact, the majority of such 3D fingering studies consider unidirectional flows in porous media (3D equivalent of the 2D rectangular Hele-Shaw cell geometry) and tackle the problem by utilizing intensive numerical simulations [40–44]. These numerical studies have demonstrated that the nonlinear tip-splitting mechanism found in 2D fingering persists to three dimensions. More recently, the numerical simulations performed in Ref. [45] have reinforced the findings of Refs. [40–44]. However, in Ref. [45] it was found that, in contrast to the 2D fingering structures obtained in Hele-Shaw cells, tip splitting into three or more branches can also be observed in 3D fingering in porous media. By the way, very recently [46] the occurrence of fingertip splitting in miscible 3D viscous fingering was experimentally detected with the use of x-ray computer tomography scanning, for unidirectional flows in a packed bed of plastic particles.

Despite the validity and relevance of the existing numerical and experimental studies carried out in Refs. [40–46] on 3D fingering of miscible fluids in porous media, the analytical understanding and description of this type of fluid dynamic system have not received much attention in the literature. One interesting exception is the work by Dias [47], who considered a 3D analog of the usual 2D radial immiscible flow that occurs in Hele-Shaw cells. In Ref. [47] Dias utilized a linear stability theory to describe the initial stages of the dynamics of a radially growing interface separating two immiscible fluids, flowing in a uniform 3D porous medium. Nevertheless, instead of focusing on the development of interfacial fingering structures, Dias concentrated on using a variational method to search for an injection rate strategy that would optimally minimize the occurrence of disturbances at the evolving interface. Therefore, a predominantly analytical study of the evolution of such a nontrivial radially expanding fluid-fluid interface in 3D porous media is still missing. Consequently, an analytical understanding of the possible occurrence of tip-splitting events in the immiscible 3D fingering system studied in Ref. [47] and the related nonlinear miscible 3D tip-splitting phenomena already reported in Refs. [40–46] is indeed lacking.

The linear stability analysis of the radially growing interface in the 3D fingering problem studied in Ref. [47] applies only to very early (linear) stages of the flow. Thus, it cannot explain the intrinsically nonlinear mechanism of fingertip splitting [1]. To properly analyze the possible emergence of this fundamentally important effect, in this work we develop the weakly nonlinear (second-order) mode-coupling theory for immiscible 3D fingering in a uniform porous medium. In this framing, we focus our attention on the onset of nonlinear effects and investigate their influence on the morphology of the perturbed fluid-fluid interface. The problem is particularly well suited to analytical treatment, permitting a relatively simple description of important stability and morphological aspects during linear and early nonlinear flow stages.

The remainder of the paper is organized as follows. Section II formulates the immiscible 3D fingering problem and derives a nonlinear ordinary differential equation that governs the early linear and nonlinear time evolution of the interfacial perturbation amplitudes. Section III discusses both linear (Sec. III A) and weakly nonlinear (Sec. III B) dynamics. It concentrates on the dawning of fingertip-broadening and fingertip-splitting phenomena. Consistently with the 2D fingering case in radial Hele-Shaw geometry [32], we show that the mechanism of fingertip splitting in immiscible 3D fingering relies on the coupling of the fundamental interface modes and their first harmonics. Our main conclusions are summarized in Sec. IV.

II. GOVERNING EQUATIONS AND THE WEAKLY NONLINEAR SCHEME

Consider the flow of two immiscible, incompressible viscous fluids in a uniform 3D porous medium. Denote the viscosities and densities of fluid 1 and fluid 2 by η_1 and ρ_1, and η_2 and ρ_2, respectively. There exists a surface tension σ between the fluids and the compositional properties of the porous medium are expressed by the permeability k. Throughout this work we will be interested in examining the formation and growth of the 3D branching patterns that arise at the fluid-fluid interface when the less viscous fluid 1 flows in a porous medium saturated with a more viscous fluid 2. Fluid 1 is injected at a constant volumetric rate Q at the origin of the coordinate system, gradually displacing the surrounding fluid 2 radially outward. Initially, the two-fluid interface is spherical and has a radius $R(t=0)=R_0$, being centered at the origin. As time progresses, the interface deforms due to the Saffman-Taylor instability. Under such circumstances, the perturbed shape of the fluid-fluid interface can be described as

$$\mathcal{R}(\theta,\phi,t) = R(t) + \zeta(\theta,\phi,t), \tag{1}$$

where $R(t)$ is the time-dependent unperturbed radius. By using volume conservation, $R(t)$ can be written as

$$R(t) = \left[R_0^3 + \frac{3}{4\pi}Qt\right]^{1/3} \tag{2}$$

and $\zeta(\theta,\phi,t)$ is the interface perturbation in spherical coordinates (θ is the polar angle and ϕ is the azimuthal angle).

The weakly nonlinear analysis we employ in this work is complementary to the related purely linear investigation performed in Ref. [47]. Here we direct attention to the intermediate dynamic stage that bridges the initial linear and the fully nonlinear regimes of the two-fluid interface evolution. Despite its importance regarding the understanding of the stability properties of the evolving interface, a purely linear theory is unable to predict and explain the nonlinear mechanism of fingertip splitting. In order to analyze this important nonlinear phenomenon in the context of 3D fingering in porous media, we use a perturbative, second-order, weakly nonlinear approach which allows access to the onset of nonlinear effects. Our perturbative analytical calculation keeps terms up to second order in ζ and considers the nonlinear coupling of fundamental modes to their harmonics. Such a weakly nonlinear perturbative scheme is analogous to the one utilized in Ref. [32] to study the emergence of pattern formation in 2D viscous fingering in a radial Hele-Shaw cell.

Owing to the spherical symmetry of the unperturbed system, it is convenient to expand the interface perturbation $\zeta(\theta,\phi,t)$ in terms of spherical harmonics as

$$\zeta(\theta,\phi,t) = \sum_{l=0}^{\infty}\sum_{m=-l}^{l}\zeta_{lm}(t)Y_{lm}(\theta,\phi), \tag{3}$$

where the spherical harmonic perturbation amplitudes are $\zeta_{lm} = \int_0^{2\pi}\int_0^{\pi} d\Omega\,\zeta(\theta,\phi,t)Y_{lm}^*(\theta,\phi)$ and $d\Omega = \sin\theta d\theta d\phi$ is the solid angle element. The integer l is related to the wavelength of the perturbation modes, whereas the integer m is associated with the direction of perturbation in three dimensions [48,49]. At this point, it is important to recall that the complex conjugate of the spherical

harmonic function Y_{lm}^* satisfies the relationship $Y_{lm}^*(\theta,\phi) = (-1)^m Y_{l-m}(\theta,\phi)$ [48]. Consequently, in order for the interface perturbation [Eq. (3)] to be real valued, it is necessary that the conjugate of the amplitudes $\zeta_{lm}(t)$ also obeys the relation $\zeta_{lm}^*(\theta,\phi) = (-1)^m \zeta_{l-m}(\theta,\phi)$. Moreover, to ensure volume conservation, the zeroth mode ($l = 0, m = 0$) must satisfy

$$\zeta_{00}(t) = -\frac{1}{\sqrt{4\pi}R} \sum_{\substack{lm \\ l\neq 0}} |\zeta_{lm}(t)|^2. \tag{4}$$

In a uniform porous medium, fluid flow is well described by Darcy's law [5]

$$\mathbf{v}_j = -\frac{k}{\eta_j}\nabla[p_j - \rho_j g z], \tag{5}$$

where the index j is 1 (2) for the displacing (displaced) fluid. The terms $\mathbf{v}_j = \mathbf{v}_j(r,\theta,\phi,t)$ and $p_j(r,\theta,\phi,t)$ are the fluids' 3D velocity and pressure, respectively. The second term in square brackets in Eq. (5) denotes the potential due to gravitational effects, where g is the acceleration of gravity. Since Eq. (5) implies that the flow is irrotational, we can define a velocity potential as $\mathbf{v}_j = -\nabla\Phi_j$. In addition, the incompressibility of the fluids requires that their velocities obey the condition $\nabla \cdot \mathbf{v}_j = 0$. Consequently, the velocity potentials must satisfy Laplace's equation in three dimensions, $\nabla^2\Phi_j = 0$, whose solutions are

$$\Phi_1(r,\theta,\phi,t) = \frac{Q}{4\pi r} + \sum_{l=1}^{\infty}\sum_{m=-l}^{l} \Phi_{1lm}(t)\left(\frac{r}{R(t)}\right)^l Y_{lm}(\theta,\phi) \tag{6}$$

for the inner fluid and

$$\Phi_2(r,\theta,\phi,t) = \frac{Q}{4\pi r} + \sum_{l=1}^{\infty}\sum_{m=-l}^{l} \Phi_{2lm}(t)\left(\frac{r}{R(t)}\right)^{-(l+1)} Y_{lm}(\theta,\phi) \tag{7}$$

for the outer fluid. Note that these expressions are consistent with the boundary conditions at $r = 0$ and ∞.

To find a relationship between the velocity potential coefficients Φ_{jlm} and the perturbation amplitudes ζ_{lm}, we apply the kinematic boundary condition [50]

$$\frac{\partial\mathcal{R}}{\partial t} = \left[\frac{1}{r^2}\frac{\partial\Phi_j}{\partial\theta}\frac{\partial\mathcal{R}}{\partial\theta} + \frac{1}{r^2\sin^2\theta}\frac{\partial\Phi_j}{\partial\phi}\frac{\partial\mathcal{R}}{\partial\phi} - \frac{\partial\Phi_j}{\partial r}\right]_{r=\mathcal{R}}, \tag{8}$$

which expresses the continuity of the normal flow velocity as one crosses from fluid 1 to fluid 2. Besides this boundary condition, two integrals involving spherical harmonics are essential to perform the calculations

$$\begin{aligned}&\int_0^{2\pi}\int_0^{\pi} d\Omega\, Y_{lm}^*(\theta,\phi)Y_{l_1m_1}(\theta,\phi)Y_{l_2m_2}(\theta,\phi)\\ &= (-1)^m\sqrt{\frac{(2l+1)(2l_1+1)(2l_2+1)}{4\pi}}\begin{pmatrix} l & l_1 & l_2\\ -m & m_1 & m_2\end{pmatrix}\begin{pmatrix} l & l_1 & l_2\\ 0 & 0 & 0\end{pmatrix},\end{aligned} \tag{9}$$

and

$$\begin{aligned}&\int_0^{2\pi}\int_0^{\pi} d\Omega\, Y_{lm}^*(\theta,\phi)\left(\frac{\partial Y_{l_1m_1}(\theta,\phi)}{\partial\theta}\frac{\partial Y_{l_2m_2}(\theta,\phi)}{\partial\theta} + \frac{1}{\sin^2\theta}\frac{\partial Y_{l_1m_1}(\theta,\phi)}{\partial\phi}\frac{\partial Y_{l_2m_2}(\theta,\phi)}{\partial\phi}\right)\\ &= (-1)^{m+1}\sqrt{\frac{(2l+1)(2l_1+1)(2l_2+1)}{4\pi}}\sqrt{l_1(l_1+1)(2l_1+1)l_2(l_2+1)(2l_2+1)}\\ &\quad\times\begin{Bmatrix} l & l_1 & l_2\\ 1 & l_1 & l_2\end{Bmatrix}\begin{pmatrix} l & l_1 & l_2\\ -m & m_1 & m_2\end{pmatrix}\begin{pmatrix} l & l_1 & l_2\\ 0 & 0 & 0\end{pmatrix},\end{aligned} \tag{10}$$

where $\begin{pmatrix} a & b & c \\ d & e & f \end{pmatrix}$ and $\begin{Bmatrix} a & b & c \\ d & e & f \end{Bmatrix}$ are the Wigner $3j$ and $6j$ symbols, respectively. The derivation of these integrals and the values of the symbols can be found in Refs. [48,51–53]. By using these integrals and Eqs. (6)–(8) we obtain

$$\begin{aligned}\Phi_{1lm}(t) = &-\frac{1}{l}\left(R\dot{\zeta}_{lm} + \frac{Q}{2\pi R^2}\zeta_{lm}\right) \\ &+ \frac{(-1)^m}{l}\sum_{l_1m_1}\sum_{l_2m_2}\sqrt{\frac{(2l+1)(2l_1+1)(2l_2+1)}{4\pi}}\begin{pmatrix} l & l_1 & l_2 \\ -m & m_1 & m_2 \end{pmatrix}\begin{pmatrix} l & l_1 & l_2 \\ 0 & 0 & 0 \end{pmatrix} \\ &\times\left(\frac{Q}{4\pi R^3}\left[2l_1+1-\frac{2}{l_1}\sqrt{l_1(l_1+1)(2l_1+1)l_2(l_2+1)(2l_2+1)}\begin{Bmatrix} l & l_1 & l_2 \\ 1 & l_1 & l_2 \end{Bmatrix}\right]\zeta_{l_1m_1}\zeta_{l_2m_2}\right. \\ &\left.+\left[l_1-1-\frac{1}{l_1}\sqrt{l_1(l_1+1)(2l_1+1)l_2(l_2+1)(2l_2+1)}\begin{Bmatrix} l & l_1 & l_2 \\ 1 & l_1 & l_2 \end{Bmatrix}\right]\dot{\zeta}_{l_1m_1}\zeta_{l_2m_2}\right)\end{aligned} \tag{11}$$

and a similar expression for $\Phi_{2lm}(t)$. The overdot in $\dot{\zeta}_{lm}$ denotes the total time derivative. The summations in l run from 1 to ∞ and the summations in m go from $-l$ to l. To make the expressions more compact, from now on all the summations in either l_1,m_1, or l_2,m_2 follow the same convention in their lower and upper limits.

The second boundary condition of importance to our 3D fingering problem expresses the pressure jump due to the curvature of the interface between the fluids. For a uniform porous medium, a modified Young-Laplace pressure jump relation was proposed by Chuoke *et al.* [5] and is given by

$$(p_1 - p_2)|_{\mathcal{R}} = 2\bar{\sigma}\mathcal{H} + p_c(t), \tag{12}$$

where $\mathcal{H}$ is the mean curvature of the interface [47,50], which in second order in ζ can be expressed as

$$2\mathcal{H} = \boldsymbol{\nabla}\cdot\left[\frac{\boldsymbol{\nabla}[r-\mathcal{R}(\theta,\phi,t)]}{|\boldsymbol{\nabla}[r-\mathcal{R}(\theta,\phi,t)]|}\right] = \frac{2}{R} - \frac{2\zeta+\nabla_\omega^2\zeta}{R^2} + \frac{2\zeta^2+2\zeta\nabla_\omega^2\zeta}{R^3} + O(\zeta^3), \tag{13}$$

with the operator ∇_ω^2 being the Laplacian restricted to the unit sphere. The effective macroscopic surface tension $\bar{\sigma}$ follows a linear relationship with the usual surface tension coefficient $\bar{\sigma} = C\sigma$ and the multiplicative factor C varies depending on the properties of the porous medium [5]. The last term on the right-hand side of Eq. (12) is related to the capillary pressure drop and will not be relevant to our analysis since it depends only on time and not on the shape of the interface. More details about this boundary condition as well as the typical experimental values of the constant C can be found in Refs. [5,47] and references therein.

To get the equation of motion for the fluid-fluid interface in our 3D setting, it is convenient to rewrite Eq. (5) for each of the fluids in terms of the velocity potential and then subtract the resulting equations from each other, evaluated at the perturbed interface $r = \mathcal{R}$, yielding

$$A\frac{\Phi_1|_{\mathcal{R}} + \Phi_2|_{\mathcal{R}}}{2} + \frac{\Phi_1|_{\mathcal{R}} - \Phi_2|_{\mathcal{R}}}{2} = -\frac{k[(p_1-p_2)-(\rho_1-\rho_2)gz]|_{\mathcal{R}}}{\eta_1+\eta_2}, \tag{14}$$

where

$$A = \frac{\eta_1-\eta_2}{\eta_1+\eta_2} \tag{15}$$

is the viscosity contrast. Since the focal point of our study is the development of 3D viscous fingering, we concentrate on the instability due to the viscosity difference between the fluids and consider that $\rho_1 \approx \rho_2$ so that gravitational effects can be neglected. In other words, we assume that $(\rho_1 - \rho_2)gz|_{\mathcal{R}} \ll (p_1 - p_2)|_{\mathcal{R}}$.

Now we have all the necessary ingredients to find a mode-coupling differential equation that describes the time evolution of the interfacial amplitudes $\zeta_n(t)$. Substituting Eq. (11) (and its equivalent for fluid 2) and the pressure jump condition (12) into Eq. (14), always keeping terms up to second order in ζ, and Fourier transforming, after some algebra we obtain the dimensionless equation of motion for the perturbation amplitudes

$$\dot{\zeta}_{lm} = \Lambda(l)\zeta_{lm} + \sum_{l_1 m_1}\sum_{l_2 m_2}\left[\mathcal{F}(l,m;l_1,m_1,l_2,m_2)\zeta_{l_1 m_1}\zeta_{l_2 m_2} + \mathcal{G}(l,m;l_1,m_1,l_2,m_2)\dot{\zeta}_{l_1 m_1}\zeta_{l_2 m_2}\right], \quad (16)$$

where

$$\Lambda(l) = \frac{2}{R^3}\left[A\frac{l(l+1)}{2l+1-A} - 1 - \frac{1}{\mathrm{Ca}}\frac{l(l+2)(l^2-1)}{2l+1-A}\right] \quad (17)$$

is the linear growth rate and

$$\mathrm{Ca} = \frac{(\eta_1+\eta_2)Q}{4\pi k\bar{\sigma}} \quad (18)$$

is the capillary number. Moreover,

$$\begin{aligned}
&\mathcal{F}(l,m;l_1,m_1,l_2,m_2)\\
&= \frac{(-1)^m}{R^4}\sqrt{\frac{(2l+1)(2l_1+1)(2l_2+1)}{4\pi}}\begin{pmatrix} l & l_1 & l_2\\ -m & m_1 & m_2\end{pmatrix}\begin{pmatrix} l & l_1 & l_2\\ 0 & 0 & 0\end{pmatrix}\\
&\times\left[A\left(\frac{2l(l+1)-(2l_1+1)(2l+1)}{2l+1-A} - 2\frac{(l+1)(l_1+1)+ll_1}{l_1(l_1+1)(2l+1-A)}\right.\right.\\
&\left.\times\sqrt{l_1(l_1+1)(2l_1+1)l_2(l_2+1)(2l_2+1)}\begin{Bmatrix} l & l_1 & l_2\\ 1 & l_1 & l_2\end{Bmatrix}\right)\\
&+\frac{2l_1+1}{2l+1-A} + 2\frac{(l+1)(l_1+1)-ll_1}{l_1(l_1+1)(2l+1-A)}\sqrt{l_1(l_1+1)(2l_1+1)l_2(l_2+1)(2l_2+1)}\\
&\left.\times\begin{Bmatrix} l & l_1 & l_2\\ 1 & l_1 & l_2\end{Bmatrix} - \frac{4}{\mathrm{Ca}}\frac{l(l+1)\left(1-l_1-l_1^2\right)}{2l+1-A}\right]
\end{aligned} \quad (19)$$

and

$$\begin{aligned}
&\mathcal{G}(l,m;l_1,m_1,l_2,m_2)\\
&= \frac{(-1)^m}{R}\sqrt{\frac{(2l+1)(2l_1+1)(2l_2+1)}{4\pi}}\begin{pmatrix} l & l_1 & l_2\\ -m & m_1 & m_2\end{pmatrix}\begin{pmatrix} l & l_1 & l_2\\ 0 & 0 & 0\end{pmatrix}\\
&\times\left[A\left(\frac{2l(l+1)-l(l_1+2)-(l+1)(l_1-1)}{2l+1-A} - \frac{(l+1)(l_1+1)+ll_1}{l_1(l_1+1)(2l+1-A)}\right.\right.\\
&\left.\times\sqrt{l_1(l_1+1)(2l_1+1)l_2(l_2+1)(2l_2+1)}\begin{Bmatrix} l & l_1 & l_2\\ 1 & l_1 & l_2\end{Bmatrix}\right)\\
&+\frac{(l+1)(l_1-1)-l(l_1+2)}{2l+1-A} + 2\frac{(l+1)(l_1+1)-ll_1}{l_1(l_1+1)(2l+1-A)}\\
&\left.\times\sqrt{l_1(l_1+1)(2l_1+1)l_2(l_2+1)(2l_2+1)}\begin{Bmatrix} l & l_1 & l_2\\ 1 & l_1 & l_2\end{Bmatrix}\right]
\end{aligned} \quad (20)$$

represent second-order mode-coupling terms. In Eq. (16) lengths are rescaled by R_0 and time by $4\pi R_0^3/Q$. It should be emphasized that, for the rest of this paper, we work with the dimensionless version of all the equations. Notice that our 3D fingering problem is conveniently described in terms

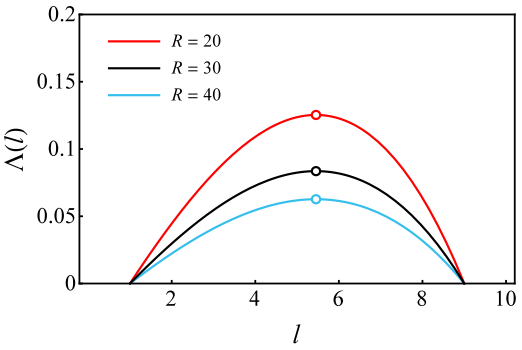

FIG. 1. Plot of the growth rate Λ as a function of l for three values of the unperturbed radius R. Here we set Ca $= 110$ and $A = 1$. The small open circles locate the most unstable mode $l_{\max}$. It is clear that variations in R do not influence the width of the band of unstable modes and the mode of maximum growth rate $l_{\max}$.

of just two dimensionless parameters: the viscosity contrast A [Eq. (15)] and the capillary number Ca [Eq. (18)].

Equations (16)–(20) constitute one of the key results of this work, offering the time evolution of the perturbation amplitudes $\zeta_n(t)$ accurate to second order for the immiscible 3D radial fingering problem in porous media. This allows us to investigate the intrinsic nonlinear morphological aspects of the emerging pattern-forming 3D fingering structures at the fluid-fluid interface. It should be noticed that, in spite of the formal similarities between the calculation performed here to derive Eqs. (16)–(20) and the more standard steps followed in Ref. [32] to get the corresponding equations for the 2D viscous fingering flow in a radial Hele-Shaw cell, Eqs. (16)–(20) are indeed quite distinct from those obtained in the 2D situation analyzed in Ref. [32] [their Eqs. (18)–(21)]. Among the distinctions are the considerably larger number of possible couplings for the modes in three dimensions and the detailed forms of nonlinear mode-coupling terms [Eqs. (19) and (20)]. Therefore, it is evident that the level of complexity of the 3D fingering equations (and, for that matter, of the 3D fingering problem itself) is significantly higher than that of their 2D counterparts. In the next section we analyze in detail the consequences of these equations for the linear stability and for the nonlinear pattern formation dynamics of viscous fingers in three dimensions.

III. DISCUSSION

A. Linear stage: Interface stability

Although the main focus of this work is on understanding the development of intrinsically nonlinear aspects of the fluid-fluid interface morphology (in particular, 3D fingertip-splitting phenomena), in this section we briefly discuss some noteworthy facts of the purely linear regime of the interface evolution. We begin by examining the linear growth rate for our 3D fingering problem [Eq. (17)]

$$\Lambda(l) = \frac{1}{R^3}\lambda(l), \tag{21}$$

where

$$\lambda(l) = 2\left[A\frac{l(l+1)}{2l+1-A} - 1 - \frac{1}{\mathrm{Ca}}\frac{l(l+2)(l^2-1)}{2l+1-A}\right]. \tag{22}$$

First of all, notice that, due to the spherical symmetry of the flow, the linear growth rate does not depend on the mode m. With the help of Fig. 1, we analyze some important features of $\Lambda(l)$. Figure 1 illustrates how the growth rate $\Lambda(l)$ varies with mode l for a characteristic capillary number Ca $= 110$ and for a common situation in which the viscosity contrast $A = 1$, meaning that the outer

fluid is much more viscous than the inner one. This is done for three increasingly larger values of the unperturbed interface radius $R = R(t)$ ($R = 20$, 30, and 40). Of course, considering three values of R is equivalent to observing the interface evolution for three different instants of time. By inspecting Fig. 1, we readily verify that, as R is varied, the band of unstable modes, defined by the range of spherical harmonic modes l for which the growth rate is positive, remains unchanged. This means that, in the linear regime, such an instability band does not change as the interface evolves. It should be stressed that this peculiar 3D fingering linear behavior is very different from the equivalent linear response observed during 2D fingering in radial Hele-Shaw cells. In fact, in radial Hele-Shaw flows one detects a phenomenon known as a cascade of modes [25,31,32], consisting of a progressive enlargement of the band of unstable modes as time progresses. This cascade of modes is one of the most iconic features of the linear regime in 2D radial fingering in Hele-Shaw flows and it is not at all present in 3D radial fingering in porous media.

We proceed by directing the readers' attention to the particularly interesting functional form assumed by Eq. (21), where the linear growth rate expression is separated as a product of the unperturbed radius $R = R(t)$ by $\lambda(l)$ [given by Eq. (22)]. An important consequence of this separation of the variables R and l is the fact that the most unstable mode (or mode of largest growth rate), calculated by setting $d\lambda(l)/dl|_{l_{\max}} = 0$, does not vary with time. For instance, if one considers the most intense viscosity-driven instability case associated with $A = 1$ (situation represented in Fig. 1), we have that

$$l_{\max} = \tfrac{1}{3}[\sqrt{3\,\mathrm{Ca} + 7} - 2], \tag{23}$$

which has no dependence on either t or $R = R(t)$. This can be checked in Fig. 1, where the value of l related to the location of the maxima of the curves (the maxima are indicated by the small open circles) remains unchanged as R is varied. This is an additional significant difference between 2D and 3D radial viscous fingering at the linear level. As a matter of fact, for 2D fingering in radial Hele-Shaw cells, where the interface perturbation is described by a Fourier series expansion, the Fourier mode with maximum growth rate (which is connected to the typical number of growing fingers on the interface) does increase with time [25,31,32]. This is in sharp contrast to what happens in 3D radial viscous fingering, where $l_{\max}$ is constant in time [Eq. (23)]. As a result, for 3D radial fingering in porous media, the number of fingerlike protuberances on the evolving interface should remain fixed during the linear stage of the dynamics.

Another differing aspect between the 3D and 2D fingering systems is related to the analytical closed-form linear solution for the interface perturbation amplitudes. In our present 3D fingering setting it is straightforward to solve the linear equation for $\zeta_{lm}(t)$ [Eq. (16)], which leads to a neat, compact expression

$$\zeta_{lm}(t) = \zeta_{lm}(0)R^{\lambda(l)} = \zeta_{lm}(0)[1 + 3t]^{\lambda(l)/3}. \tag{24}$$

Note that $\zeta_{lm}(t)$ has a simple power-law (algebraic) dependence on R which is considerably different from the more involved, dominantly exponential dependence observed in the corresponding linear solution for the 2D viscous fingering problem in radial Hele-Shaw cells [25,31,32].

We conclude this linear section by discussing the combined role of the viscosity contrast A and the capillary number Ca in determining the linear stability of the 3D fingering problem. This is done in Fig. 2, which presents a linear stability diagram for the system in the parameter space A-Ca, showing the stable and unstable regions of the linear dynamics. The stable region is colored in white. The boundary between the two regions depicted in Fig. 2 is obtained by setting $\lambda(l_{\max}) = 0$. From Eq. (24) one realizes that below (above) this separating curve, the amplitude $\zeta_{lm}(t)$ decreases (increases) as time advances. In Fig. 2 one finds that when A and Ca are sufficiently small, the interface is stable, assuming a spherical shape (see the stable region of Fig. 2). It is also evident that for larger values of Ca (a more unstable situation), higher values of A are needed to destabilize the interface. A characteristic linearly deformed 3D pattern-forming morphology is illustrated in the unstable region of Fig. 2.

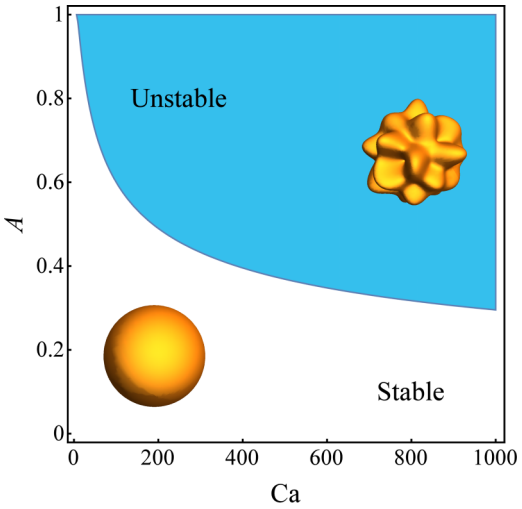

FIG. 2. Stability diagram $A-\mathrm{Ca}$ illustrating linearly stable and unstable regions of 3D viscous fingering. The boundary separating the two regions is calculated by setting $\lambda(l_{\max}) = 0$. The 3D patterns illustrate the shape of two typical fluid-fluid interfaces that arise at the linear regime during 3D fingering formation in porous media.

It is important to note that, because of the particular time dependence of the growth rate [Eq. (21)], the curve separating stable and unstable regions in the stability diagram illustrated in Fig. 2 does not change with time. Therefore, if the interface is stable at the beginning of the linear evolution, it will remain stable irrespective of the duration of the injection process. One more time, this 3D fingering behavior is in striking contrast to the corresponding conduct during 2D fingering formation: In radial Hele-Shaw flows, the band of unstable modes increases with time, so for finite values of Ca and A the system eventually becomes unstable, as long as the injection process lasts a sufficiently long time.

We close this section by commenting on the main differences and similarities between the linear stability analysis for 3D radial viscous fingering performed in Ref. [47] and the one we carried out in this work. In Ref. [47], Dias derived an expression for the linear growth rate for the special case in which $A = 1$, but instead of investigating its main physical implications for the stability of the system focused on using it to employ a variational approach and obtain an optimal time-dependent injection rate that minimizes interfacial perturbations. In contrast, in this work we derived a slightly more general expression for the growth rate [Eq. (17)], now valid for arbitrary values of A, and explored its role in the linear stability of the fluid-fluid interface. As discussed throughout this section, our current 3D linear stability analysis revealed some interesting features that are dissimilar to the ones observed in its 2D counterpart (i.e., traditional Saffman-Taylor problem in radial Hele-Shaw cells). Examples of these important linear findings are (i) the detection of algebraic growth for the interfacial disturbances [see Eq. (24)] and (ii) the observation of certain regions of absolute stability for finite values of A and Ca (see Fig. 2). None of these relevant facts were examined in Ref. [47].

B. Nonlinear stage: Morphology of fingering patterns

Consider now the second term on the right-hand side of Eq. (16), which represents the weakly nonlinear (second-order) contribution to the flow. Unlike the linear case, in which different modes grow independently of each other, the weakly nonlinear terms introduce couplings among the various different modes. These couplings drive the growth of modes that are not dynamically active in the linear stage and these emergent modes are in turn responsible for the development of distinctive

morphological features, such as fingertip broadening and fingertip splitting. To visualize the onset of these pattern-forming features, first it is necessary to solve the system of coupled differential equations described by Eq. (16). This can be done in two ways: (i) by solving the coupled equations numerically or (ii) by substituting the linear solution given by Eq. (24) (and its time derivative) into the second-order terms on the right-hand side of Eq. (16) and then integrating the resulting expression to obtain the solution analytically. These two ways are equivalent, since they differ only by third-order terms that are discarded in our analysis. Here we choose the second approach and write the nonlinear coupling term as

$$W(l,m,t) = \sum_{l_1 m_1} \sum_{l_2 m_2} [\mathcal{F}(l,m;l_1,m_1,l_2,m_2) + \Lambda(l)\mathcal{G}(l,m;l_1,m_1,l_2,m_2)]\zeta^{lin}_{l_1 m_1}\zeta^{lin}_{l_2 m_2}, \tag{25}$$

where ζ^{lin}_{lm} denotes the linear perturbation amplitudes given by Eq. (24). Thus, the differential equation for each of the mode amplitudes ζ_{lm} becomes

$$\dot{\zeta}_{lm} = \Lambda(l)\zeta_{lm} + W(l,m,t), \tag{26}$$

which is just a first-order differential equation with a forcing term $W(l,m,t)$, which can be integrated, yielding

$$\zeta_{lm}(t) = \zeta^{lin}_{lm}(t)\left\{1 + \int_0^t \left[\frac{W(l,m,t')}{\zeta^{lin}_{lm}(t')}\right]dt'\right\}. \tag{27}$$

The explicit expression for the integral appearing in Eq. (27) is very cumbersome in the 2D fingering case [32] and therefore is not of much analytical use. However, in our current 3D fingering situation the integral can be promptly evaluated in a straightforward manner. First, we note that it is possible to separate the time dependence in the expressions for the couplings functions $\mathcal{F}(l,m;l_1,m_1,l_2,m_2)$ and $\mathcal{G}(l,m;l_1,m_1,l_2,m_2)$, given in Eqs. (19) and (20) as

$$\mathcal{F}(l,m;l_1,m_1,l_2,m_2) = \frac{1}{[R(t)]^4}F(l,m;l_1,m_1,l_2,m_2) \tag{28}$$

and

$$\mathcal{G}(l,m;l_1,m_1,l_2,m_2) = \frac{1}{R(t)}G(l,m;l_1,m_1,l_2,m_2). \tag{29}$$

Then, by defining two auxiliary functions

$$T(l,m;l_1,m_1,l_2,m_2) = F(l,m;l_1,m_1,l_2,m_2) + \lambda(l)G(l,m;l_1,m_1,l_2,m_2) \tag{30}$$

and

$$I(l;l_1,l_2,t) = R(t)^{\lambda(l)}\int_0^t R(t')^{\lambda(l_1)+\lambda(l_2)-\lambda(l)-4}dt' = \frac{R(t)^{\lambda(l_1)+\lambda(l_2)-1} - R(t)^{\lambda(l)}}{\lambda(l_1)+\lambda(l_2)-\lambda(l)-1}, \tag{31}$$

the full second-order solution can be simply expressed as

$$\zeta_{lm}(t) = \zeta_{lm}(0)R^{\lambda(l)} + \sum_{l_1 m_1}\sum_{l_2 m_2} T(l,m;l_1,m_1,l_2,m_2)I(l;l_1,l_2,t)\zeta_{l_1 m_1}(0)\zeta_{l_2 m_2}(0). \tag{32}$$

This solution contains all the necessary information required to analyze the viscous fingering pattern formation in 3D porous media. Additionally, by inspecting Eq. (32) it is possible to see that, even if all modes have the same initial amplitude, there exists an explicitly dependence on m due to $T(l,m;l_1,m_1,l_2,m_2)$ and consequently the degeneracy in m present in the linear solution for the amplitudes is broken at the weakly nonlinear level.

The expression (32) contains a summation over all the infinite couplings between all l_1, m_1, l_2, and m_2. Fortunately, it is possible to reduce the number of couplings while performing the summation,

by considering certain selection rules, i.e., conditions for which $T(l,m;l_1,m_1,l_2,m_2) \neq 0$, which are given by

$$m = m_1 + m_2, \tag{33}$$

$$|l_1 - l_2| \leqslant l \leqslant l_1 + l_2, \tag{34}$$

and

$$l + l_1 + l_2 \text{ is an even integer.} \tag{35}$$

These rules are due to the Wigner $3j$ symbols selection rules [54]. The first rule [Eq. (33)] is identical to the selection rule for the coupling terms in the 2D fingering case [32]. However, the remaining two rules [Eqs. (34) and (35)] have no 2D counterpart. Also, since Eqs. (34) and (35) are not strict equalities, the number of couplings in the 3D problem is much larger than in the corresponding 2D situation. To better illustrate this point, consider a situation in which the initial perturbation consists in just one perturbation mode. For a 2D viscous fingering system, the second-order effects will cause this initial mode (say, mode n) to drive the growth of only one additional mode, namely, its first harmonic $2n$ [32]. The situation is very different for a 3D fingering problem, in which, for instance, the mode with amplitude ζ_{40} can alone affect the growth of four other modes (ζ_{80}, ζ_{60}, ζ_{40}, and ζ_{20}) during the second-order weakly nonlinear evolution. Due to these important distinctions, it is not possible to do a direct comparison between the 2D weakly nonlinear case studied in Ref. [32] and our fully 3D viscous fingering in porous media. Moreover, this implies that, rigorously speaking, there is no way to foresee the shape of an evolving 3D fingering fluid-fluid interface just on the basis of what happens during the evolution of two-fluid interfaces in the corresponding 2D fingering system. So, to properly scrutinize the shape of the emerging 3D fingering structures, it is necessary to obtain plots of such fluid-fluid interfaces from scratch.

To visualize the onset of pattern formation for 3D fingering in porous media, we plot interfaces for different initial conditions and for different values of the governing physical parameters Ca and A. Furthermore, we note that from this point on we illustrate our results focusing on the popular maximum viscosity contrast situation ($A = 1$). This is justified by the fact that we have verified that the only effect of reducing A (i.e., of taking $0 \leqslant A < 1$) is to delay or to suppress completely the occurrence of viscous fingering. These two possible scenarios can be explained on the grounds of a purely linear analysis (Sec. III A) and have no significant implications for the understanding of the nonlinear pattern morphologies. While plotting the interfaces shown in Figs. 3–5 and 7, we stop the time evolution of the patterns as soon as the base of the fingers starts to move inward, which would make successive interfaces cross one another. Since this crossing is observed neither in 2D viscous fingering experiments in Hele-Shaw cells [23–25] nor in 3D simulations [40–44] of flows in porous media, as in Ref. [55] we adopt the largest time [or, equivalently, the largest unperturbed radius R; see Eq. (2)] before crossing as the upper bound time (R) for the validity of our theoretical description. The usefulness and effectiveness of this criterion have been demonstrated in Ref. [55] for the 2D case. The same argument used in Ref. [55] can also be applied to the 3D case. Therefore, the final times (or R's) of all plots we present in this work are determined by using this condition. We have also verified the validity of the weakly nonlinear approach by checking that the amplitudes of the second-order corrections, which can be estimated by the ζ_{00} in Eq. (4), are always much smaller than the unperturbed radius ($\zeta_{00} \ll R$).

We initiate our discussion by analyzing Fig. 3, which displays various fluid-fluid interfaces, considering the coupling of modes with $2 \leqslant l \leqslant 16$. In Fig. 3 we depict interfaces in which the initial conditions consist only of modes with $l = 3$, i.e., the initial amplitudes are given by $|\zeta_{lm}| = 0.03$ if $l = 3$ and $|\zeta_{lm}| = 0$ otherwise. In addition, since the amplitudes are complex valued, we choose random phases for the initial amplitude of each mode. By doing that, we guarantee that we are not setting a preferential direction that could bias our results. Applying the selection rules to this situation, one finds that, at the weakly nonlinear level, the participating modes are ζ_{6m}, ζ_{4m}, ζ_{3m}, and ζ_{2m}, where

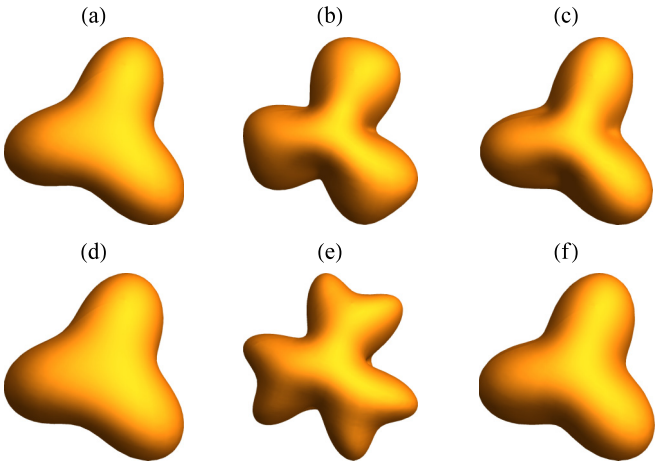

FIG. 3. Plot of typical 3D fingering interfaces for which initial conditions only contain modes with $l = 3$: (a) and (d) the purely linear interfaces, (b) and (e) the equivalent nonlinear interfaces, and (c) and (f) the same nonlinear interfaces shown in (b) and (e) but with the mode with $l = 6$ removed. The patterns illustrated in (a)–(c) used $\mathrm{Ca} = 60$ and $R = 500$, while the structures displayed in (d)–(f) utilized the parameters $\mathrm{Ca} = 80$ and $R = 50$.

all possible m's must be considered. Thus, notice that despite the fact that initially only the mode with $l = 3$ is present, due to the nonlinear couplings set by the selection rules, modes with $l = 6$, 4, 3, and 2 are all present at the weakly nonlinear stage. The same type of observations are applied to Figs. 4 and 5. We have plotted interfaces for a large number of different phases and amplitudes and found that the great majority of the patterns obtained have the same basic morphological features as the ones shown in Fig. 3. In this sense, one can say that the patterned structures illustrated in Fig. 3 are pretty typical.

In Figs. 3(a)–3(c) all interfaces are plotted by setting $\mathrm{Ca} = 60$ and $R = 500$. Figure 3(a) represents a purely linear interface, while Fig. 3(b) is the equivalent weakly nonlinear interface. Comparing these

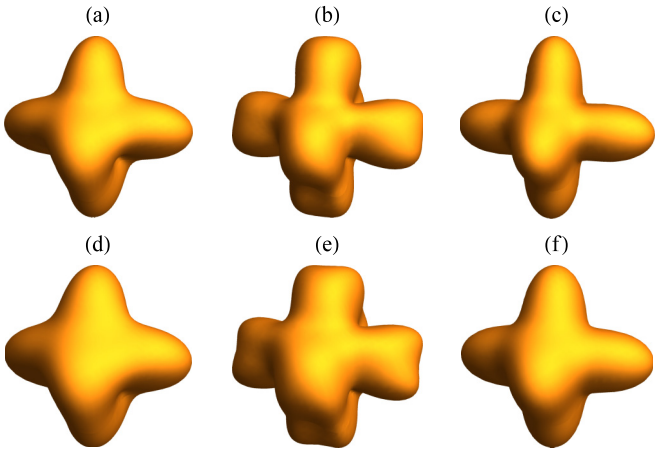

FIG. 4. Plot of characteristic 3D fingering interfaces for which initial conditions only contain modes with $l = 4$: (a) and (d) the purely linear interfaces, (b) and (e) the corresponding nonlinear interfaces, Finally, and (c) and (f) the same nonlinear interfaces shown in (b) and (e) but with the mode with $l = 8$ filtered out. The patterns illustrated in (a)–(c) used $\mathrm{Ca} = 110$ and $R = 105$, while the structures displayed in (d)–(f) utilized the parameters $\mathrm{Ca} = 130$ and $R = 57.5$.

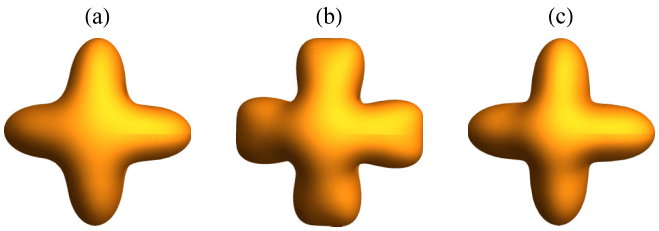

FIG. 5. The 3D fingering interfaces for Ca $= 110$, $R = 80$, $l = 4$, and $m = 4$: (a) the purely linear interface, (b) the weakly nonlinear interface, and (c) the weakly nonlinear interface, where the mode a_{88} has been removed.

two interfaces, we see that the linear situation exhibits a simple threefold pattern, having fingerlike structures presenting relatively narrow tips. In contrast, the nonlinear situation reveals a pattern having wider fingers, with blunt tips. These findings indicate that such fingertip-broadening behavior is induced by nonlinear effects. In order to identify which mode, among those driven by the nonlinear dynamics, promotes the widening effect, in Fig. 3(c) we show a filtered out, weakly nonlinear interface, containing all modes but that with $l = 6$, which has been removed. As it turns out, the filtered out interface illustrated in Fig. 3(c) does not present any of the tip-widening features detected in Fig. 3(b) and it is in fact fairly similar to the purely linear interface depicted in Fig. 3(a). This suggests that the modes having $l = 6$ (curiously, the double of the $l = 3$ set by the initial condition) play a major role in determining the emergence of such fingertip-broadening characteristics. Despite the apparent resemblance with the corresponding 2D fingertip-broadening mechanism studied in Ref. [32], this 3D fingering result is a bit surprising since after the application of the selection rules, one realizes that the interface shown in Fig. 3(c) contains all modes with $l = 2,3,4$. These values of l correspond to 20 different spherical harmonics. Nevertheless, due to the particularities of the 3D system, modes with $l = 2$ and $l = 4$ do not experience a large growth.

We advance by examining the 3D fingering patterns depicted in Figs. 3(d)–3(f) which are generated for a larger value of the capillary number than that used in Figs. 3(a)–3(c). First, we notice that increasing the value of Ca has almost no effect on the linear patterns produced [i.e., patterns illustrated in Figs. 3(a) and 3(d) are pretty similar to one another]. However, the tendency toward a stronger tip-broadening effect, or even the occurrence of fingertip-splitting events, is observed when a larger value of the capillary number is used. This can be seen by comparing Fig. 3(b) (obtained by setting Ca $= 60$) and the equivalent weakly nonlinear pattern shown in Fig. 3(e) (generated for Ca $= 80$). The nonlinear pattern shown in Fig. 3(e) has much broader fingers and displays a clear tip-splitting formation, with two small secondary fingers emerging from a large one. This sort of fingertip-splitting behavior is one of the most emblematic features of the 2D fingering situation. Finally, Fig. 3(f) plots the same weakly nonlinear interface depicted in Fig. 3(e) but without including the modes with $l = 6$. The lack of any tip splitting and tip broadening in Fig. 3(f) confirms that indeed the modes with $l = 6$ are responsible for the main morphological features in this 3D case. This 3D behavior has some interesting similarities to the 2D case, where a first-harmonic mode $2n$ is driven (via a weakly nonlinear coupling) by its fundamental mode n, leading to fingertip-splitting formation [32]. Even so, it should be pointed out that in our current 3D case, instead of the presence of a single first harmonic the system actually has various first harmonics, namely, all the modes with $l = 6$, and different associated values of m.

Regarding the filtering process used in Figs. 3(c) and 3(f), we point out that if any other modes (other than $2l$) are removed from the dynamic description of the interface, one just observes very small subtle changes in the resulting morphology of the patterns. Most importantly, if these other modes are filtered out, one definitely does not detect any significant alteration in the phenomena of fingertip broadening and fingertip splitting. Curiously, this suggests that, despite the differences between 2D and 3D fingering, the basic weakly nonlinear mechanism leading to tip broadening and fingertip splitting in both systems is fundamentally the same, i.e., it is ruled by the coupling between

a fundamental mode l and its first harmonic $2l$. These statements are also valid for the patterns obtained in Figs. 4, 5, and 7.

To test the validity and robustness of the conclusions reached in the analysis of Fig. 3 for $l = 3$, in Fig. 4 we perform a similar analysis for another value of l, namely, $l = 4$. The interfaces shown in Figs. 4(a)–4(c) are obtained by setting $\mathrm{Ca} = 110$ and $R = 105$, whereas the interfaces shown in Figs. 4(d)–4(f) are generated by setting $\mathrm{Ca} = 130$ and $R = 57.5$. All patterns are produced by considering that $2 \leqslant l \leqslant 16$ for the same initial perturbation $\zeta_{lm}(0) = 0.0009$ and for a random choice of phases. After utilizing the selection rules to this situation, we obtain that the participating modes are ζ_{8m}, ζ_{6m}, ζ_{4m}, and ζ_{2m}, where all possible m's must be taken into account. Similar to the case with $l = 3$ discussed in Fig. 3, we see that the linear fourfold interfaces in Figs. 4(a) and 4(d) have narrow fingers compared to broader fingers that arise in the equivalent nonlinear cases shown in Figs. 4(b) and 4(e). Moreover, by removing the mode $l = 8$, all the morphologically relevant nonlinear effects disappear, as can be seen by examining Figs. 4(c) and 4(f). Furthermore, fingertip broadening is detected in Fig. 4(b), while fingertip splitting is noticeable in Fig. 4(e), confirming that these phenomena take place no matter what value of l is considered. In fact, we have verified that patterns similar to those shown in Figs. 3 and 4 also arise in 3D fingering interfaces produced by starting from initial perturbation amplitudes having l equal to 2, 5, 6, and 7.

While it was found in Figs. 3 and 4 that modes $2l$, the first harmonics of mode l, are responsible for the occurrence of fingertip-broadening and fingertip-splitting phenomena, it is worth noting that the patterns depicted in these figures start from a highly degenerate initial state, containing many m's. Thus, it is not really possible to gain much analytical insight from these situations. For instance, it is not clear how each mode set by the pair (l,m), corresponding to a perturbation amplitude ζ_{lm}, contributes to the overall shape of the nonlinear patterns. To investigate this issue further, we consider a situation where initially only one mode ζ_{lm} is present. For this analysis, it is convenient to introduce real amplitudes $a_{lm} = \zeta_{lm} + \zeta_{lm}^*$ and $b_{lm} = i(\zeta_{lm} - \zeta_{lm}^*)$. Moreover, we can choose, without loss of generality, the initial phase of the mode so that $a_{lm} > 0$ and $b_{lm} = 0$. In Fig. 5 we plot the 3D fingering interfaces generated for $l = 4$, $m = 4$, initial amplitude $a_{44} = 0.0047$, capillarity number $\mathrm{Ca} = 110$, and $R = 80$. By comparing the linear [Fig. 5(a)] and the weakly nonlinear [Fig. 5(b)] interfaces, it is apparent that nonlinear effects favor the broadening and eventual splitting of the fingers. Additionally, in Fig. 5(c), the mode a_{88} is taken out from the interface evolution and the nonlinear effects related to broadening and splitting vanish. Despite the evidence extracted from Figs. 3 and 4, it should be clear that the removal of the specific mode a_{88} in Fig. 5(c) was a result of a trial and error process, since, in principle, we had no particular formal reason to believe that this mode was the one responsible for favoring broadening and splitting events. Notice that a_{88} is not the only mode having $l = 8$. For instance, the mode a_{80} also participates in the dynamics, but does not contribute much to the emergence of such morphological features. By the way, after applying the selection rules, one concludes that the participating modes are a_{80}, a_{60}, a_{44}, a_{40}, and a_{20}.

To reinforce the conclusions reached by analyzing Fig. 5, the variation of the mode amplitudes a_{44} and a_{88} as R is increased is shown in Fig. 6 for two values of Ca. As expected, we see that, by increasing the capillarity number, the growth of both mode amplitudes a_{44} and a_{88} is favored. However, the increase in the harmonic mode amplitude a_{88} due to the change in Ca is much stronger, increasing by 130% compared to an increase of about 30% in a_{44}. This is consistent with Figs. 3 and 4, where we see that the tip splitting becomes indeed more salient for larger values of Ca, even though the overall finger length does not vary significantly. Actually, by using Eq. (32) it is possible to express the time dependence of the cosine mode amplitude a_{2l2m} (under the influence of mode a_{lm}) simply as

$$a_{2l2m}(t) = a_{2l2m}(0)[R(t)]^{\lambda(2l)} + \tfrac{1}{2}T(2l,2m;l,m,l,m)I(2l;l,l,t)a_{lm}^2(0). \tag{36}$$

Since $a_{lm}^2(0) > 0$ and $I(2l;2l,2l,t) > 0$ [see Eq. (31)], Eq. (36) shows that the sign of the mode amplitude of $a_{2l2m}(t)$ is entirely governed only by the function $T(2l,2m;l,m,l,m)$. By performing some simulations, we have been able to verify that if $a_{2l2m} > 0$, the tip of the fingers become sharp,

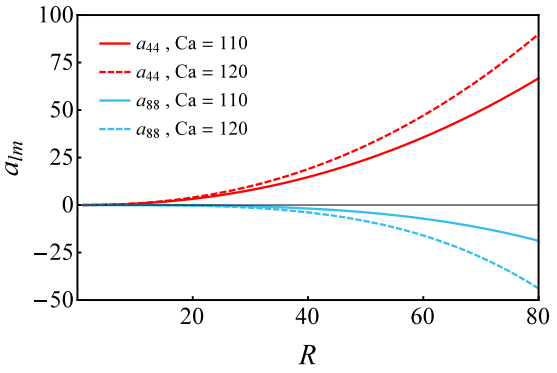

FIG. 6. Variation of (a) the fundamental mode cosine amplitude a_{44} and (b) the harmonic mode cosine amplitude a_{88}, as R is increased. This is done for two values of the capillary number: Ca = 110 (solid curves) and Ca = 120 (dashed curves).

whereas if $a_{2l2m} < 0$, the fingertips become wider. Therefore, one can predict the dynamic response of the fingertip just by examining the behavior of such a controlling function. Incidentally, this analysis is valid for all times during the weakly nonlinear evolution, since the function $T(2l,2m;l,m,l,m)$ does not depend on time. Thus, it is indeed possible to mimic all the relevant physics associated with the onset of the fingering pattern formation in 3D porous media by just considering two modes, namely, a_{lm} and a_{2l2m}.

Figures 5 and 6 have focused on an illustrative case, for which $l = 4$ and $m = 4$. Nonetheless, one can reach very similar conclusions no matter what mode is chosen as the initial condition. In fact, we have verified that even if different initial choices of l and m are made, a process of fingertip broadening, possibly followed by a fingertip-splitting event, is detected. These processes are caused by the influence of a fundamental mode a_{lm} on its first-harmonic mode a_{2l2m}, which acquires negative amplitudes and whose growth obeys Eq. (36). However, irrespective of the fact that all 3D fingering cases rely on the same underlying physical mechanism, there are some interesting differences in the actual interfacial pattern morphologies generated by different values of l and m. For example, in Fig. 5 for $l = 4$ and $m = 4$, we see the emergence of a conventional fingertip-splitting phenomenon, resulting in two small fingers. However, if one takes different values of m, for instance, $m = 3$ and $m = 2$, not all fingers split into two secondary fingers and it is actually possible to observe splitting into three secondary fingers.

Figure 7 illustrates some different morphologies that may arise during a 3D tip-splitting event. Figures 7(a) and 7(b) show interfaces for $l = 3$, $R = 30$, Ca = 90, and initial amplitude $|\zeta_{lm}| = 0.03$. In contrast, Figs. 7(c) and 7(d) display interfaces for $l = 4$, $R = 50$, Ca = 150, and initial amplitude $|\zeta_{lm}| = 0.0009$. In addition, similar to what was done in Figs. 3 and 4, the interfaces shown in Fig. 7 contain all modes m for a given l. Furthermore, each pattern presented has been produced by utilizing different phases. By comparing Figs. 7(a) and 7(b) we see that the former exhibits a typical tip splitting, resulting in only two secondary fingers, while the latter reveals a more peculiar type of pattern, in which three small fingers emerge from the tip of each larger finger. A similar phenomenon can be seen in the second row of Figs. 7(c) and 7(d), where we compare two interfaces having the same $l = 4$ but different initial phases. The phases in Fig. 7(c) favor the growth of modes that cause traditional tip splitting into two lobes, whereas the random phases set in Fig. 7(d) favor the growth of modes that generate a three-lobed fingertip-splitting structure. It should be stressed that these distinct patterns are just different manifestations of the same tip-splitting mechanism, as discussed previously in this work, and no new physical effect is present. Moreover, it should be noted that the patterns displayed in Figs. 7(b) and 7(d) are not a result of an artifact due to the random phases associated with various participating m's. As a matter of fact, we have observed two- and

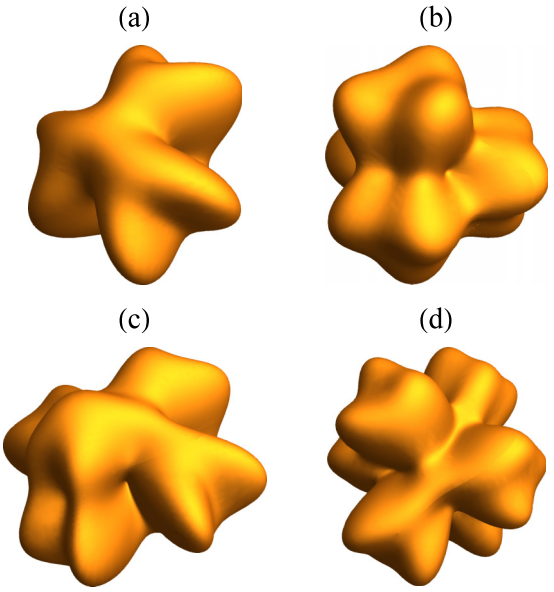

FIG. 7. The 3D fingering interfaces showing different types of fingertip-splitting patterns: (a) and (b) interfaces having $l = 3$, $\mathrm{Ca} = 90$, and the same initial amplitude $|\zeta_{lm}| = 0.03$ but different initial phases and (c) and (d) interfaces having $l = 4$, $\mathrm{Ca} = 150$, and the same initial amplitude $|\zeta_{lm}| = 0.0009$ but different initial phases. One can identity (a) and (c) traditional two-lobed tip splitting and (b) and (d) a more peculiar three-lobed tip splitting.

three-lobed splitting even in cases where only one mode m is present in the initial condition and no random phase is assumed.

The existence of a tip-splitting phenomenon involving two or three fingers has also been recently reported in the literature [45] in a theoretical study that used numerical simulations to examine fully nonlinear stages of 3D fingering in porous media. Actually, the simulations carried out in Ref. [45] have found tip splitting into more than three secondary fingers. Nevertheless, by using our weakly nonlinear analysis, we have obtained finger splitting into just two or three secondary fingers. This may be caused by the fact that the equations and flow geometric arrangement utilized in the numerical work performed in Ref. [45] are a bit different from the ones we use in our current paper. Additionally, there is also the possibility that tip splitting into more than three fingers is a fully nonlinear effect and therefore could not be assessed by a perturbative, second-order weakly nonlinear approach.

We conclude by commenting on some important issues related to our modal analysis. Recent works have used nonmodal stability analysis to describe 3D hydrodynamic flows in porous media. For example, nonmodal growth has been observed in linear viscous fingering flows for miscible fluids [56] and in density-driven convection resulting from dissolution of CO_2 [57]. In these studies a mathematical coupling between the velocity and the concentration fields is found through the action of convection and diffusion. This type of advection-diffusion system is well known to possess a stability matrix with a nonorthogonal eigenvector basis [58]. These basic features characterize the so-called nonmodal growth. It has been shown that, under such specific conditions, algebraic growth of perturbations can be detected [59].

Nevertheless, the physical system we investigate in this work is much simpler than the ones examined in Refs. [56–59]. In our investigation, the fluids are immiscible, thus convection and diffusion are not present. In addition, it is worth pointing out that Eq. (3) is not simply an ansatz but a general expansion of the perturbation function in the (complete) basis of spherical harmonics. By means of this expansion, we are able demonstrate that, at linear level, the associated stability matrix

is diagonal for all times [see Eq. (16) without the nonlinear terms] and therefore the linearized system is normal. Furthermore, despite the somewhat unexpected nature of some of our linear results, as mentioned earlier, our weakly nonlinear predictions, in particular those associated with the tip-splitting phenomenon, are consistent with the 3D numerical simulations presented in Ref. [45]. The consistency between our weakly nonlinear results [which, by the way, make use of the linear perturbation amplitudes as indicated in Eqs. (25)–(27)] and the numerical findings of Ref. [45] supports the validity of our modal analysis.

IV. CONCLUSION

The celebrated Saffman-Taylor (viscous fingering) instability is most commonly observed in confined fluid flows that take place in the effectively 2D geometry of a Hele-Shaw cell. In this setting, 2D fingering emerges when a fluid displaces another of higher viscosity. These 2D fingerlike structures grow and eventually split at their tips, leading to the development of archetypal fingertip-splitting events which gives rise to complex branched patterns. Such interfacial patterns have been extensively studied in the literature through experiments and theory (via analytical and numerical methods) in both rectangular and radial Hele-Shaw cell setups.

The viscous fingering instability can also arise in three dimensions. One of the most important examples of 3D fluid fingering involves two phase flows in porous media. An emblematic instance of this type of fluid dynamic system, of great practical and economic relevance, is the flow associated with enhanced oil recovery processes. Interestingly, the overwhelming majority of studies in 3D fingering focus on unidirectional flows, the 3D counterpart of the 2D fingering situation that happens in rectangular (or channel) Hele-Shaw cells. In addition, almost all such investigations probe the occurrence of 3D fingertip-splitting events via numerical simulations.

In this work, however, we studied the 3D fingering instability and the emergence of fingertip-splitting phenomena when a fluid displaces a more viscous one radially outward in a uniform 3D porous media. In this framework we analyzed the 3D analog of 2D viscous fingering in a radial Hele-Shaw cell. Moreover, instead of concentrating on complicated numerical techniques, we tackled the problem in a predominantly analytical fashion. We employed a perturbative, weakly nonlinear analysis that utilized a second-order mode-coupling approach to get useful insight into the linear stability of the fluid-fluid interface and the mechanism of fingertip-splitting formation in our 3D radial fingering setting. Already at the linear level, we identified important distinctions between the 3D and 2D radial fingering: (i) While in two dimensions interfacial perturbation is mostly dictated by exponential growth, in three dimensions algebraic growth is detected; in addition, (ii) while in two dimensions the system eventually becomes unstable for finite values of A and Ca, in three dimensions there exists a stable region for finite values of these physical parameters. At the weakly nonlinear level, our results indicated that, similarly to the 2D fingering situation, the 3D fingertip-splitting mechanism relies on the nonlinear coupling of fundamental modes and their first harmonics. Nevertheless, in contrast to what is normally detected in 2D radial fingering, we have found that in 3D fingering, tip splitting can also occur involving the branching of three secondary fingers.

Still within the scope of fluid flows in 3D porous media, a natural extension of the current work would be the use of the weakly nonlinear theory to examine the onset of fingering and pattern formation in a 3D axisymmetric tube geometry (i.e., a 3D Saffman-Taylor problem in a tube), as originally proposed and investigated numerically in a different context by Levine and Tu in Ref. [60]. Outside the realm of flows in porous media, but still in a 3D environment, our second-order mode-coupling approach could also be useful to try to understand the onset of nonlinearities in the 3D viscous fingering instabilities that arise in toroidal droplets, as recently investigated experimentally and via linear stability analysis in Ref. [61]. Finally, as another possible target system to which our weakly nonlinear scheme can be applied, we mention the formation of Laplacian branching patterns during electric discharges in 3D streamers [62]. In this last case, our second-order perturbative method could provide valuable analytical information about the basic nonlinear physical mechanisms leading

to the generation of the convoluted, 3D treelike electric discharge patterns, analyzed so far mostly by numerical simulations.

ACKNOWLEDGMENTS

J.A.M. thanks CNPq (Brazilian Research Council) for financial support through Grant No. 304821/2015-2. E.O.D. acknowledges financial support from FACEPE through PPP Project No. APQ-0800-1.05/14.

[1] For review articles on this subject see G. M. Homsy, Viscous fingering in porous media, Annu. Rev. Fluid Mech. **19**, 271 (1987); K. V. McCloud and J. V. Maher, Experimental perturbations to Saffman-Taylor flow, Phys. Rep. **260**, 139 (1995); J. Casademunt, Viscous fingering as a paradigm of interfacial pattern formation: Recent results and new challenges, Chaos **14**, 809 (2004).
[2] S. Hill, Channelling in packed columns, Chem. Eng. Sci. **1**, 247 (1952).
[3] P. G. Saffman and G. I. Taylor, The penetration of a fluid into a porous medium or Hele-Shaw cell containing a more viscous liquid, Proc. R. Soc. London Ser. A **245**, 312 (1958).
[4] H. Lamb, *Hydrodynamics* (Dover, New York, 1945).
[5] R. L. Chuoke, P. van Meurs, and C. van der Poel, The instability of slow, immiscible, viscous liquid-liquid displacements in permeable media, Petroleum Trans. AIME **216**, 188 (1959).
[6] P. Zhuravlev, Shape of interface in fluids displacement, Zap Leningrad Com. Inst. **133**, 54 (1956).
[7] L. W. Lake, *Enhanced Oil Recovery* (Prentice Hall, Englewood Cliffs, 1989).
[8] B. Metz, O. Davidson, H. De Connick, M. Loos, and L. Meyer, *IPCC Special Report on Carbon Dioxide Capture and Storage* (Cambridge University Press, New York, 2005).
[9] J. S. Langer, Dendrites, viscous fingers, and the theory of pattern formation, Science **243**, 1150 (1989).
[10] O. Zik, Z. Olami, and E. Moses, Fingering Instability in Combustion, Phys. Rev. Lett. **81**, 3868 (1998).
[11] H.-Y. Chu and H.-K. Lee, Evolution of the Plasma Bubble in a Narrow Gap, Phys. Rev. Lett. **107**, 225001 (2011).
[12] A. C. Callan-Jones, J.-F. Joanny, and J. Prost, Viscous-Fingering-Like Instability of Cell Fragments, Phys. Rev. Lett. **100**, 258106 (2008).
[13] C. Blanch-Mercader and J. Casademunt, Spontaneous Motility of Actin Lamellar Fragments, Phys. Rev. Lett. **110**, 078102 (2013).
[14] C. Giverso, M. Verani, and P. Ciarletta, Branching instability in expanding bacterial colonies, J. R. Soc. Interface **12**, 20141290 (2015).
[15] R. A. Wooding, Growth of fingers at an unstable diffusing interface in a porous medium or Hele-Shaw cell, J. Fluid Mech. **39**, 477 (1969).
[16] G. Tryggvason and H. Aref, Numerical experiments on Hele-Shaw flow with a sharp interface, J. Fluid Mech. **136**, 1 (1983).
[17] J. V. Maher, Development of Viscous Fingering Patterns, Phys. Rev. Lett. **54**, 1498 (1985).
[18] T. Maxworthy, The nonlinear growth of a gravitationally unstable interface in a Hele-Shaw cell, J. Fluid Mech. **177**, 207 (1987).
[19] E. Meiburg and G. M. Homsy, Nonlinear unstable viscous fingers in Hele-Shaw flows. II. Numerical simulation, Phys. Fluids **31**, 429 (1988).
[20] J. A. Miranda and M. Widom, Weakly nonlinear investigation of the Saffman-Taylor problem in a rectangular Hele-Shaw cell, Int. J. Mod. Phys. B **12**, 931 (1998).
[21] C. Jiao and T. Maxworthy, An experimental study of miscible displacement with gravity-override and viscosity contrast in Hele-Shaw cell, Exp. Fluids **44**, 781 (2008).
[22] B. Jha, L. Cueto-Felgueroso, and R. Juanes, Fluid Mixing from Viscous Fingering, Phys. Rev. Lett. **106**, 194502 (2011).

[23] J. Bataille, Stabilité d'un écoulement radial non miscible, Rev. Inst. Fr. Pet. Ann. Combust. Liq. **23**, 1349 (1968).
[24] S. D. R. Wilson, A note on the measurement of dynamic contact angles, J. Colloid Interface Sci. **51**, 532 (1975).
[25] L. Paterson, Radial fingering in a Hele-Shaw cell, J. Fluid Mech. **113**, 513 (1981).
[26] L. Paterson, Fingering with miscible fluids in a Hele-Shaw cell, Phys. Fluids **28**, 26 (1985).
[27] S. N. Rauseo, P. D. Barnes, and J. V. Maher, Development of radial fingering patterns, Phys. Rev. A **35**, 1245 (1987).
[28] J. D. Chen, Radial viscous fingering patterns in Hele-Shaw cells, Exp. Fluids **5**, 363 (1987).
[29] J. D. Chen, Growth of radial viscous fingers in a Hele-Shaw cell, J. Fluid Mech. **201**, 223 (1989).
[30] H. Thomé, M. Rabaud, V. Hakim, and Y. Couder, The Saffman-Taylor instability: From the linear to the circular geometry, Phys. Fluids A **1**, 224 (1989).
[31] S. S. S. Cardoso and A. W. Woods, The formation of drops through viscous instability, J. Fluid Mech. **289**, 351 (1995).
[32] J. A. Miranda and M. Widom, Radial fingering in a Hele-Shaw cell: A weakly nonlinear analysis, Physica D **120**, 315 (1998).
[33] O. Praud and H. L. Swinney, Fractal dimension and unscreened angles measured for radial viscous fingering, Phys. Rev. E **72**, 011406 (2005).
[34] P. Fast and M. J. Shelley, Moore's law and the Saffman-Taylor instability, J. Comput. Phys. **212**, 1 (2006).
[35] C.-Y. Chen, C.-W. Huang, H. Gadêlha, and J. A. Miranda, Radial viscous fingering in miscible Hele-Shaw flows: A numerical study, Phys. Rev. E **78**, 016306 (2008).
[36] S. W. Li, J. S. Lowengrub, J. Fontana, and P. Palffy-Muhoray, Control of Viscous Fingering Patterns in a Radial Hele-Shaw Cell, Phys. Rev. Lett. **102**, 174501 (2009).
[37] I. Bischofberger, R. Ramanchandran, and S. R. Nagel, Fingering versus instability in the limit of zero surface tension, Nat. Commun. **5**, 5265 (2014).
[38] I. Bischofberger, R. Ramanchandran, and S. R. Nagel, An island of stability in a sea of fingers: Emergent global features of the viscous-flow instability, Soft Matter **11**, 7428 (2015).
[39] J. Y. Y. Chui, P. de Anna, and R. Juanes, Interface evolution during radial miscible viscous fingering, Phys. Rev. E **92**, 041003(R) (2015).
[40] W. B. Zimmerman and G. M. Homsy, Three-dimensional viscous fingering: A numerical study, Phys. Fluids **4**, 1901 (1992).
[41] M. A. Christie, A. H. Muggeridge, and J. J. Barley, 3D simulation of viscous fingering and WAG schemes, SPE Reservoir Eng. **8**, 19 (1993).
[42] H. A. Tchelepi, F. M. Orr, Jr., N. Rakotomalala, D. Salin, and R. Wouméni, Dispersion, permeability heterogeneity and viscous fingering: Acoustic experimental observations and particle tracking simulations, Phys. Fluids A **5**, 1558 (1993).
[43] H. A. Tchelepi and F. M. Orr, Jr., Interaction of viscous fingering, permeability inhomogeneity and gravity segregation in three dimensions, SPE Reservoir Eng. **9**, 266 (1994).
[44] M. Ruith and E. Meiburg, Miscible rectilinear displacements with gravity override. Part 1. Homogeneous porous medium, J. Fluid Mech. **420**, 225 (2000).
[45] M. Belotserkovskaya and A. Konyukhov, Numerical simulation of viscous fingering in porous media, Phys. Scr. **T142**, 014056 (2010).
[46] T. Suekane, J. Ono, A. Hyodo, and Y. Nagatsu, Three-dimensional viscous fingering of miscible fluids in porous media, Phys. Rev. Fluids **2**, 103902 (2017).
[47] E. O. Dias, Viscous-fingering minimization in uniform three-dimensional porous media, Phys. Rev. E **88**, 063007 (2013).
[48] G. B. Arfken, H.-J. Weber, and F. E. Harris, *Mathematical Methods for Physicists: A Comprehensive Guide* (Academic, Oxford, 2013).
[49] A. Ben-Menahem and S. J. Singh, *Seismic Waves and Sources* (Springer, New York, 2011).
[50] R. E. Rosensweig, *Ferrohydrodynamics* (Dover, New York, 2014).
[51] A. G. de Beer and S. Roke, Nonlinear Mie theory for second-harmonic and sum-frequency scattering, Phys. Rev. B **79**, 155420 (2009).

[52] R. W. James, A review of basic computations with spherical harmonics in geomagnetism, Pure Appl. Geophys. **111**, 2273 (1973).
[53] R. W. James, New tensor spherical harmonics, for application to the partial differential equations of mathematical physics, Philos. Trans. R. Soc. London Ser. A **281**, 195 (1976).
[54] A. Messiah, *Quantum Mechanics* (North-Holland, Amsterdam, 1991).
[55] M. J. P. Gingras and Z. Rácz, Noise and the linear stability analysis of viscous fingering, Phys. Rev. A **40**, 5960 (1989).
[56] T. K. Hota, S. Pramanik, and M. Mishra, Nonmodal linear stability analysis of miscible viscous fingering in porous media, Phys. Rev. E **92**, 053007 (2015).
[57] S. Rapaka, S. Chen, R. J. Pawar, P. H. Stauffer, and D. Zhang, Non-modal growth of perturbations in density-driven convection in porous media, J. Fluid Mech. **609**, 285 (2008).
[58] L. N. Trefethen and M. Embree, *Spectra and Pseudospectra: The Behavior of Nonnormal Matrices and Operators* (Princeton University Press, Princeton, 2005).
[59] T. K. Hota, S. Pramanik, and M. Mishra, in *First Complex Systems Digital Campus World E-Conference, Tempe, 2015*, edited by P. Bourgine, P. Collet, and P. Parrend, Springer Proceedings in Complexity (Springer, Cham, 2017), pp. 109–115.
[60] H. Levine and Y. Tu, Mean-field diffusion-limited aggregation and the Saffman-Taylor problem in three-dimensions, Phys. Rev. A **45**, 1044 (1992).
[61] A. A. Fragkopoulos, A. Aizenman, and A. Fernández-Nieves, Charged-Induced Saffman-Taylor Instabilities in Toroidal Droplets, Phys. Rev. Lett. **118**, 264501 (2017).
[62] M. Arrayás, M. A. Fontelos, and U. Kindelán, Onset of treelike patterns in negative streamers, Phys. Rev. E **86**, 066407 (2012).